ISSN 1349-1113
JAXA-RR-10-001E

JAXA Research and Development Report

Validation of Computational Results of Rotor/Fuselage Interaction Analysis Using *rFlow3D* Code

Yasutada TANABE, Shigeru SAITO and Ippei OTANI

May 2010

Japan Aerospace Exploration Agency

Validation of Computational Results of Rotor/Fuselage Interaction Analysis Using *rFlow3D* Code

Yasutada TANABE*[1], Shigeru SAITO*[1] and Ippei OTANI*[2]

Abstract

A newly developed rotor flow solver: *rFlow3D* is applied to an isolated helicopter fuselage in the freestream, and then to a rotor/fuselage combination to analyze the surrounding flow field and study the effects due to the rotor/fuselage interaction. The modified SLAU scheme, which stands for Simple Low-dissipative AUSM (Advection Upstream Splitting Method), is a type of locally preconditioned numerical scheme. It enables the solver to calculate realistic drag coefficient values even at low speeds under Mach 0.01 as well as those at transonic speeds. This favorable feature of the scheme is suitable for the challenging demands for predicting the flow fields surrounding helicopters. The solver is based on overlapped grid approach. The ROBIN type fuselage was adopted as the geometry for both the isolated fuselage and rotor/fuselage simulations. Experimental settings for the controls and other conditions are used in the calculations. The resulting flow field variables were then compared to the experimental measurements. It was concluded that the newly developed code provides satisfactory results. Flow features around the rotor blade root and in other low speed areas are improved and test calculations to date are promising for future applications in the analysis of flow fields surrounding helicopters.

Keywords: Helicopter, CFD, SLAU scheme, Overlapped grids, *rFlow3D*

概　　要

新規に開発された回転翼流れ場ソルバー *rFlow3D* が一様流に配置された単独胴体，およびロータ・胴体の組み合わせに対して適用され，周囲の流れ場及びロータ・胴体間の干渉現象が解析された．導入された SLAU スキームは Simple Low-dissipative AUSM (Advection Upstream Splitting Method) の略であり，局所前処理数値スキームの一種である．ヘリコプタのロータ・ブレードのような移動変形する物体周りの流れ場にも対応できるように，原型の SLAU スキームに対して，若干修正を加えた．このスキームの導入によりマッハ 0.01 以下という極低速域と遷音速域での正確な抗力係数値を同時に計算することが可能になった．この良好な特性はヘリコプタ周辺の複雑な流れ場の予測に適していると考えられている．ソルバーは重合格子を利用し，単独胴体及びロータ・胴体の組み合わせの両シミュレーションにおいて ROBIN 型胴体が適用された．制御変数や条件の設定値については実験の値がそのまま使われ，流れ場の計算出力値は実験のそれと比較された．新しく開発されたソルバーにより十分な結果が得られた．ロータ・ブレード付け根，その他の低速域での流れ場の解析精度は改善され，現時点におけるテスト計算の結果は満足できるものであり，ヘリコプタ周辺の流れ場解析への将来の適用にも期待できるものである．

＊ 1　Japan Aerospace Exploration Agency, Chofu, Tokyo, Japan
＊ 2　Tokyo Business Service Co., Ltd., Tokyo, Japan

NOMENCLATURE

A_1	blade lateral cyclic pitch angle [degrees]
B_1	blade longitudinal cyclic pitch angle [degrees]
C_P	pressure coefficient
C_T	rotor thrust coefficient
C_T/σ	rotor thrust coefficient/solidity
$\mathbf{F}$	flux through control surface
M	Mach number
M_{tip}	blade tip Mach number
M_∞	freestream Mach number
$\mathbf{R}$	flux component through control surface
S	boundary surface
$\mathbf{U}$	flow velocity vector within control volume
V	control volume
c	sonic speed
e	specific energy
g	SLAU scheme function
h	enthalpy
$\dot{m}$	mass flow rate
$\mathbf{n}$	normal vector pointing outward
p	pressure
s	cell interface area
t	time
u	flow velocity component
v	flow velocity component
$\mathbf{v}$	flow velocity vector
w	flow velocity component
$\dot{\mathbf{x}}$	moving grid velocity
x	normal vector component
y	normal vector component
z	normal vector component
Φ	numerical flux component vector
α	implicit scheme parameter (or) angle of attack
α_S	shaft angle
β	SLAU scheme switching function
β_0	coning angle
γ	ratio of specific heats
θ_0	blade collective pitch angle
μ	advance ratio
ρ	density
χ	SLAU scheme switching function

1. INTRODUCTION

The flow field surrounding helicopters is highly complicated, being unsteady in nature and having numerous separation points due to its generally complex geometry. In addition, such flow fields in question comprise a wide range of speeds, from almost zero to over Mach 0.9, for example, due to the speed difference between the rotor blade root and the blade tip in forward flight. In order to be successfully applied to an entire helicopter configuration containing the main and tail rotors plus the fuselage, and determine the effects of the rotor/fuselage interaction, the computational scheme needs not only to be time accurate, but also to be able to handle the wide speed range that exists in helicopter flights.

The newly developed *rFlow3D* solver adopts a modified version of the SLAU scheme [1-3] (which stands for Simple Low-dissipative AUSM (Advection Upstream Splitting Method) [4]) conceived by Shima in JAXA. The adoption of this scheme allows negation of the undesired effects of numerical dissipation which cause unrealistic divergence of the drag coefficient at very low Mach numbers, thus improving the accuracy of the calculation of the flow field that comprises a wide range of velocities, from almost zero to transonic.

After successful preliminary validation of the newly developed code through application to conventional two dimensional drag prediction problems [5], the *rFlow3D* code was used as an Euler solver to predict the pressure coefficients at the surface of an isolated ROBIN model helicopter fuselage without rotor in a single grid first. Successively, the computational domain was defined using an overlapped grid system, first for an isolated fuselage again, and then for a rotor-fuselage combination. For the cases with rotors, three different flight conditions with advance ratios of μ = 0.012, 0.15 and 0.23 are calculated. The experimental settings of controls and other flight conditions are used without trim adjustment at this stage. The flow field variables were validated by comparing these to existing experimental results obtained by wind tunnel testing [6, 7].

2. FLOW SOLVER

2.1 Computational Scheme

The flow solver used to compute the flow field is an Euler solver implementing the Finite-Volume-Method. The governing Euler equations in an Arbitrary Lagrangian-Eulerian (ALE) formulation [8] are

$$\frac{\partial}{\partial t}\int_{V(t)}\mathbf{U}dV + \int_{S(t)}\mathbf{F}\cdot\mathbf{n}dS = 0 \tag{1}$$

where

$$\mathbf{U}=\begin{pmatrix}\rho\\ \rho\mathbf{v}\\ \rho e\end{pmatrix},\quad \mathbf{F}=\begin{pmatrix}(\mathbf{v}-\dot{\mathbf{x}})\cdot\mathbf{n}\rho\\ (\mathbf{v}-\dot{\mathbf{x}})\cdot\mathbf{n}\rho\mathbf{v}+p\mathbf{n}\\ (\mathbf{v}-\dot{\mathbf{x}})\cdot\mathbf{n}\rho e+p\mathbf{v}\cdot\mathbf{n}\end{pmatrix}=\hat{\mathbf{F}}-\mathbf{U}\dot{\mathbf{x}}$$

Here $V(t)$ is the moving control volume and $S(t)$ is the boundary surface surrounding the volume and $\mathbf{n}$ is the normal vector to the surface pointing outward from the control volume, where $\mathbf{v}$ is the velocity of the flow, and $\dot{\mathbf{x}}$ is the velocity of the moving grid. ρ is density, p is pressure, and e is the specific total energy. For a perfect gas, $p=(\gamma-1)\rho(e-\frac{1}{2}\mathbf{v}\cdot\mathbf{v})$ is the state equation of gas, and for air, the ratio of specific heats is $\gamma=1.4$.
The sonic speed c is obtained as $c=\sqrt{\gamma\frac{p}{\rho}}$.
Applying the Finite-Volume-Method to Eq.(1), considering the averaged value of $\mathbf{U}$ inside the control volume V, we have

$$\frac{\partial(V\mathbf{U})}{\partial t}+\mathbf{R}=0 \tag{2}$$

with

$$\mathbf{R}=\int_{S(t)}\mathbf{F}\cdot\mathbf{n}dS \tag{3}$$

At cell i, a family of two-levels implicit scheme for Eq.(2) can be written as:

$$\frac{V_i^{n+1}\mathbf{U}_i^{n+1}-V_i^n\mathbf{U}_i^n}{\Delta t}+(1-\alpha)\mathbf{R}_i^{n+1}+\alpha\mathbf{R}_i^n=0 \tag{4}$$

where n is the time level and when $\alpha=0$, Eq.(4) is the backward Euler method with first order in time. When $\alpha=\frac{1}{2}$, it becomes a Crank-Nicolson method with second order in time.

$$\mathbf{R}_i=\sum_{j\in N(i)}\widetilde{\mathbf{F}}_{ij}s_{ij} \tag{5}$$

is a discretized form of $\mathbf{R}$ for cell i in Eq.(3), where $N(i)$ means the neighbor cells of cell i, and $\tilde{\mathbf{F}}_{ij}$ is the numerical flux from cell i to a neighbor cell j and S_{ij} is the area interfacing cell i and cell j. To satisfy the Geometry Conservation Law (GCL), a common grid velocity for face (ij) between time step n to $n+1$ can be defined as

$$\begin{aligned}&\left(v_n\right)_{ij}^{n+1/2}=\left[\dot{\mathbf{x}}\cdot\mathbf{n}\right]_{ij}^{n+1/2}\\ &\left[\dot{\mathbf{x}}\cdot\mathbf{n}\right]_{ij}^{n+1/2}=\left(\frac{V_i^{n+1}-V_i^n}{\Delta t}\right)_j\Big/\left((1-\alpha)s_{ij}^{n+1}+\alpha s_{ij}^{n}\right)=\frac{\Delta V_{ij}^{n+1/2}}{\Delta t\left((1-\alpha)s_{ij}^{n+1}+\alpha s_{ij}^{n}\right)}\end{aligned} \tag{6}$$

where $\Delta V_{ij}^{n+1/2}$ is the swept volume by face S_{ij} from time level n to time level $n+1$. It must be noted that α is included in Eq.(6).

There are many schemes to obtain the numerical flux in Eq.(5). In the AUSM (Advection Upstream Splitting Method)–type scheme [4],

$$\widetilde{\mathbf{F}}=\frac{\dot{m}+|\dot{m}|}{2}\mathbf{\Phi}^L+\frac{\dot{m}-|\dot{m}|}{2}\mathbf{\Phi}^R+\tilde{p}\mathbf{N} \tag{7}$$

Original SLAU scheme [1, 2] is extended to a moving grid [3] as

$$\mathbf{\Phi}=\begin{pmatrix}1\\ u\\ v\\ w\\ h\end{pmatrix},\ \text{and}\ \ \mathbf{N}=\begin{pmatrix}0\\ x_n\\ y_n\\ z_n\\ v_n\end{pmatrix} \tag{8, 9}$$

with

$$h=(e+p)/\rho \tag{10}$$

v_n calculated with Eq.(6) must be used to satisfy the GCL.

$$\begin{aligned}\tilde{p}=&\frac{p^L+p^R}{2}+\frac{\beta^+-\beta^-}{2}(p^L-p^R)\\ &+(1-\chi)(\beta^++\beta^--1)\frac{p^L+p^R}{2}\end{aligned} \tag{11}$$

$$\beta^{\pm}=\begin{cases}\frac{1}{4}\left(2\mp M^{\pm}\right)\left(M^{\pm}\pm1\right)^2, & \left|M^{\pm}\right|<1\\ \frac{1}{2}\left(1+sign(\pm M^{\pm})\right), & \text{otherwise}\end{cases} \tag{12}$$

$$M^+=\frac{V_n^L-v_n}{\bar{c}} \tag{13}$$

$$M^-=\frac{V_n^R-v_n}{\bar{c}} \tag{14}$$

$$\chi=(1-\hat{M})^2 \tag{15}$$

$$\hat{M}=\min\left(1.0,\frac{1}{\bar{c}}\sqrt{\frac{(V_n^L-v_n)^2+(V_n^R-v_n)^2}{2}}\right) \tag{16}$$

$$\dot{m}=\frac{1}{2}\left(\rho^L\left(V_n^L+\left|V_n\right|_{\max}^{+}\right)+\rho^R\left(V_n^R-\left|V_n\right|_{\max}^{-}\right)-\frac{\chi}{\bar{c}}\Delta p\right) \tag{17}$$

$$\left|V_n\right|_{\max}^{\pm}=(1-g)\left|V_n\right|_{\max}+g\left|V_n\right|^{\pm} \tag{18}$$

$$g=-\max(\min(M^+,0),-1)\cdot\min(\max(M^-,0),1) \tag{19}$$

$$\left|V_n\right|_{\max}=\max(\left|V_n\right|^+,\left|V_n\right|^-) \tag{20}$$

$$\Delta p=p^R-p^L \tag{21}$$

$$\bar{c} = \frac{1}{2}\left(c^L + c^R\right) \tag{22}$$

Here the speed normal to the face is calculated as

$$V_n = x_n u + y_n v + z_n w. \tag{23}$$

Eq.(16) is modified from the original form [1] to use the perpendicular velocity component instead of the local total speed at the cell face.

A Fourth-order Compact MUSCL TVD (FCMT) interpolation method [11] is used to obtain the L (Left) and R (Right) values at the interfacing face. This resulted in a fourth order spatial resolution while the favorable TVD (Total Variations Diminishing) property is retained.

Dual-time stepping is implemented using either the LU-SGS (Lower-Upper Symmetric Gauss-Seidel) method [12] or the DP-LUR (Data-Parallel Lower-Upper Relaxation) method [13]. Test cases in this paper were mostly computed using the JAXA Super computer System (JSS) and for efficient parallel computing, DP-LUR was mainly used. The combination of SLAU scheme with LU-SGS or DP-LUR implicit solver has been tested extensively and found to be considerably stable and suitable for a wide range of flow speeds [3]. Tri-linear interpolation was used for data exchange between the overlapping grids [14].

The SHUS scheme that had been applied until recently has some shortcomings, as its numerical dissipation caused unrealistic diversion of its computational results at very low Mach numbers. A two-dimensional drag computation of the NACA 0012 airfoil indicated that the results of the SHUS scheme tended to diverge below Mach numbers close to 0.1 [1-3]. As this is an inviscid Euler computation, idealistic drag of the airfoil at low Mach numbers must converge to zero (d'Alembert's paradox), but in real computations, drag is actually introduced as numerical errors. The SLAU scheme, in contrast, provides lower and stable drag coefficient values even at very low speeds under Mach 0.01 as well as at high speeds over Mach 1 (Fig. 1.) The favorable trait of this computational scheme is considered to be well suited to the challenging demands for predicting the flow field surrounding helicopters.

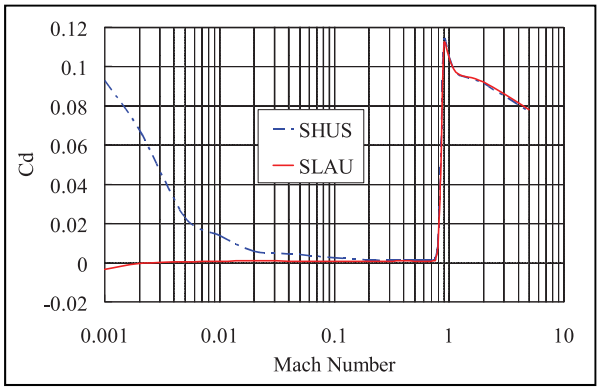

Fig. 1 NACA 0012 Drag vs. Mach Number

2.2 Grids

For this study, two types of grids were used to define the computational domain. In the preliminary case for computations of the flow field around an isolated fuselage, a single grid was used. Next, the same isolated fuselage was defined within an overlapped grid having outer and inner Cartesian background grids, and a body fitted structured grid. The calculation results were checked against the single grid results. Finally, in order to analyze the fluid dynamic interaction between the rotor and the fuselage, the flow field surrounding a rotor/fuselage combination

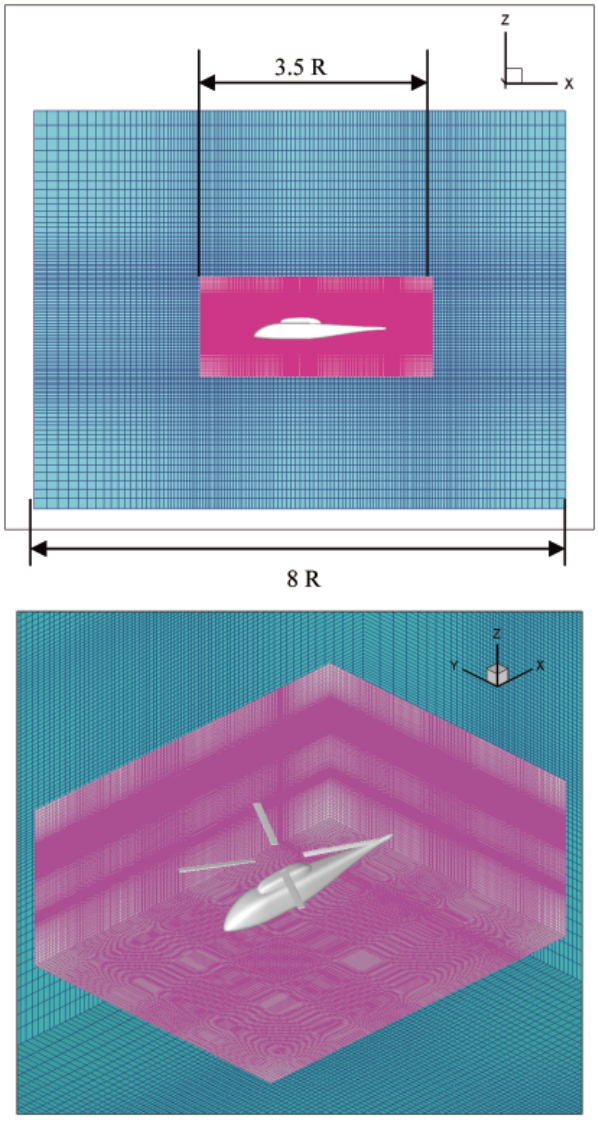

Fig. 2 The overlapping grids used for ROBIN configurations

was predicted using a moving overlapped grid.

The single body-fitted structured grid that was used for the first case of the computation of the flow field around the isolated fuselage has 101 surface grid points both in the longitudinal and radial directions, and the domain extends to a diameter, which is approximately ten times the length of the fuselage.

The overlapped grid currently in use at JAXA consists of outer and inner background grids, of which both of them have a Cartesian structure as shown in Fig. 2. The outer background grid has a length of 8 times the rotor radius and the inner background grid has a length of about 3.5 times the rotor radius. In addition, each component such as the fuselage or separate rotor blade is body-fitted with a structured grid. The moving grid technique is adopted for the blade grids, which have an O-type shape and 101 surface grid points both in the longitudinal and radial directions. These components rotate around a predefined axis within the inner background grid while undergoing prescribed feathering, flapping and lead-lagging motions.

3. ROBIN EXPERIMENTAL SETUP

3.1 ROBIN Fuselage

The ROtor-Body-INteraction (ROBIN) geometry was selected for the fuselage. This geometry, which was developed at NASA, is analytically derived with super-ellipse equations [6]. Its shape is detailed enough to depict a realistic helicopter fuselage although it is only analytically described, thus it is rendered easy to define within computation domains. The fuselage was defined by implementing such equations in a geometry generating code. The ROBIN fuselage has been extensively used both in experiments and computational simulations. The abundance of resulting data makes it an ideal choice for validating CFD codes.

For the isolated fuselage simulation, the GRMS (General Rotor Model System) version of the ROBIN fuselage was used for the analysis. This is the version reported in the experiment measurements for the fuselage surface pressure coefficients [6]. The simulation including the rotor is modeled after the IRTS (Isolated Rotor Test System) version, which is used in the wind tunnel tests measuring fuselage on-surface flow field variables under the influence of the rotor at defined flight condition parameters [7].

Fig. 3 above shows the GRMS configuration of the ROBIN fuselage and the positions where the surface pressure coefficient measurements were collected. The experimental results of time-averaged fuselage pressure measurements with no rotor are reported by Freeman and Mineck [6], where the purpose of the investigation was to provide a database for analysis verification.

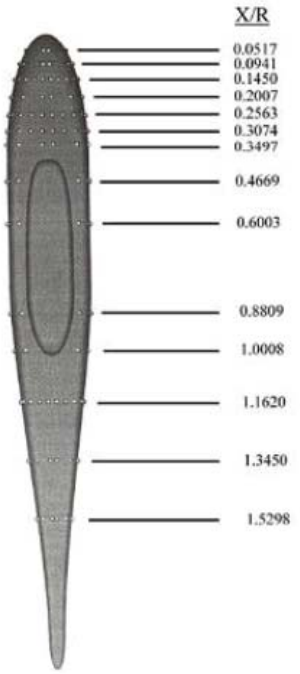

Fig. 3 ROBIN pressure tap positions [6, 7]

3.2 Flow Conditions

The steady pressure coefficient measurements were conducted for the ROBIN (GRMS version) fuselage together with computational simulations under the following conditions: Mach number of 0.062, angle of attack of 0 and -5 degrees, respectively. For the rotor/fuselage interaction study, flight condition parameters such as the advance ratio and the thrust coefficient were used to simulate the experimental conditions in the original NASA report [6]. First, the control parameters of the rotor blade were kept fixed at which the discrepancy between the experimental and computational values were then compared.

4. COMPUTATIONAL RESULTS

4.1 Isolated Fuselage Pressure Coefficients

For the computation of the isolated fuselage case, the resulting streamlines on the body surface at angles of attack of 0 and -5 degrees respectively, were visualized as in Fig. 4. Since the

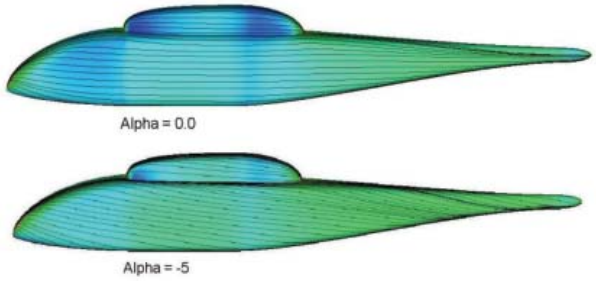

Fig. 4 Fuselage surface streamlines

simulation was executed using an Euler solver, the effects expected due to viscosity, like flow separation at blunt ends, are not present. Nonetheless the streamlines are realistic and compare well with results obtained from other computational solvers [15].

The pressure coefficients on the fuselage surface are computed for angles of attack of 0 and -5 degrees, respectively, and its values at each of the longitudinal cross-section positions given in Fig. 3 were plotted to be compared with the experimental results given by Freeman and Mineck [6], and also with the computational results obtained and reported by Chaffin and Berry [15]. The computational results by Chaffin and Berry are calculated by a vortex panel method software, *VSAERO* and a Navier Stokes solver developed at NASA, called *CFL3D*, respectively. The obtained results for the angles of attack of 0 and -5 degrees are shown in Figs. 5 and 6, respectively.

At cross sections positioned relatively in front, separation is not expected and the experimental and computational results overlap for the most part and agree very closely. Even where the cross sections are situated across the engine housing, though there is a small difference, the two sets of values match closely. At positions near the end of the engine housing, as shown in the last four graphs of Figs. 5 and 6, some amount of discrepancy becomes evident. It is highly likely that separation is occurring due to the blunt aft end of the engine housing and the wind tunnel model strut, which was not modeled in the numeric simulations. All three sets of computational results agree with each other very closely, even in the manner of the discrepancies seen in the aft portions of the fuselage.

In addition to the on-surface pressure coefficient distributions at predetermined cross sectional stations, the C_p distribution along the longitudinal centerline of the fuselage was visualized as shown for the case of $\alpha = 0$ degree in Fig. 7. The pressure coefficient distribution along the fuselage centerline has no abrupt jump in values and oscillations. The graph shows stagnation points at both front and aft ends of the fuselage and the engine housing, as it is to be expected from an Euler solver.

4.2 Rotor Fuselage Configuration

After verifying the validity of the computational scheme by applying it to the isolated fuselage case, the main rotor was included in the computations to proceed to the studies on its interaction with the fuselage. The rotor geometry was taken from the Mineck and Gorton paper [7] in order to simulate the wind tunnel test and to make comparison with the corresponding experimental results possible. This particular version of the ROBIN fuselage model is designated as the IRTS (Independent Rotor Test System) version, and its geometry features are shown

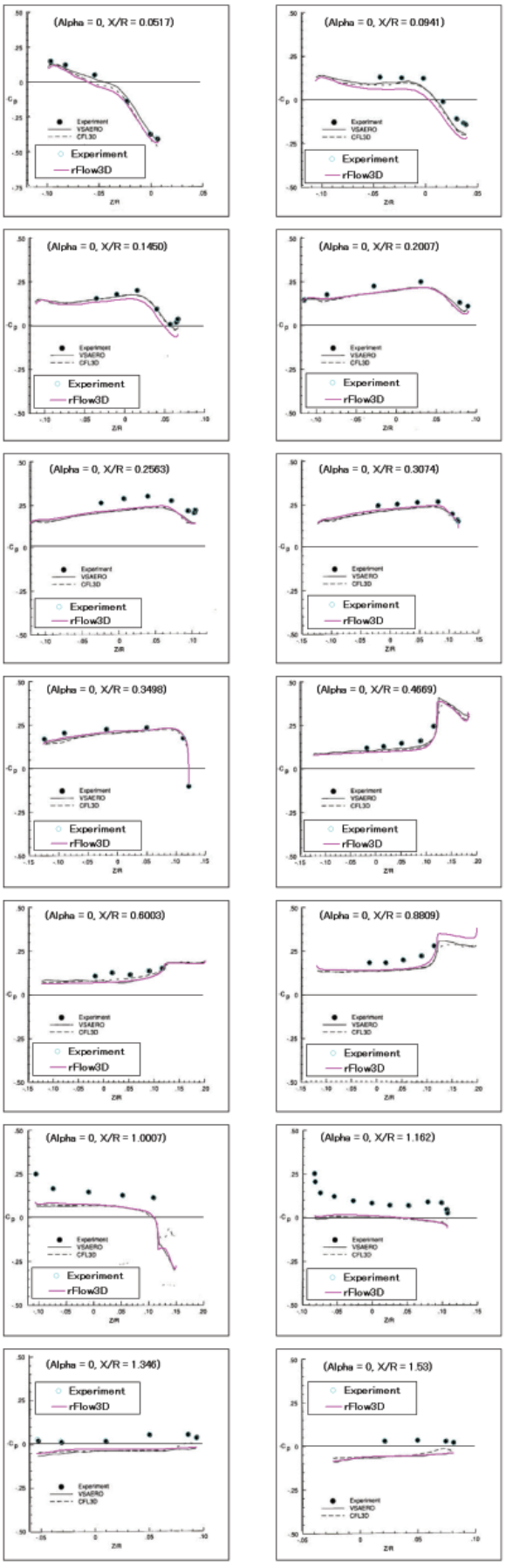

Fig. 5 Isolated fuselage surface pressure coefficients for $\alpha = 0^\circ$ [9]

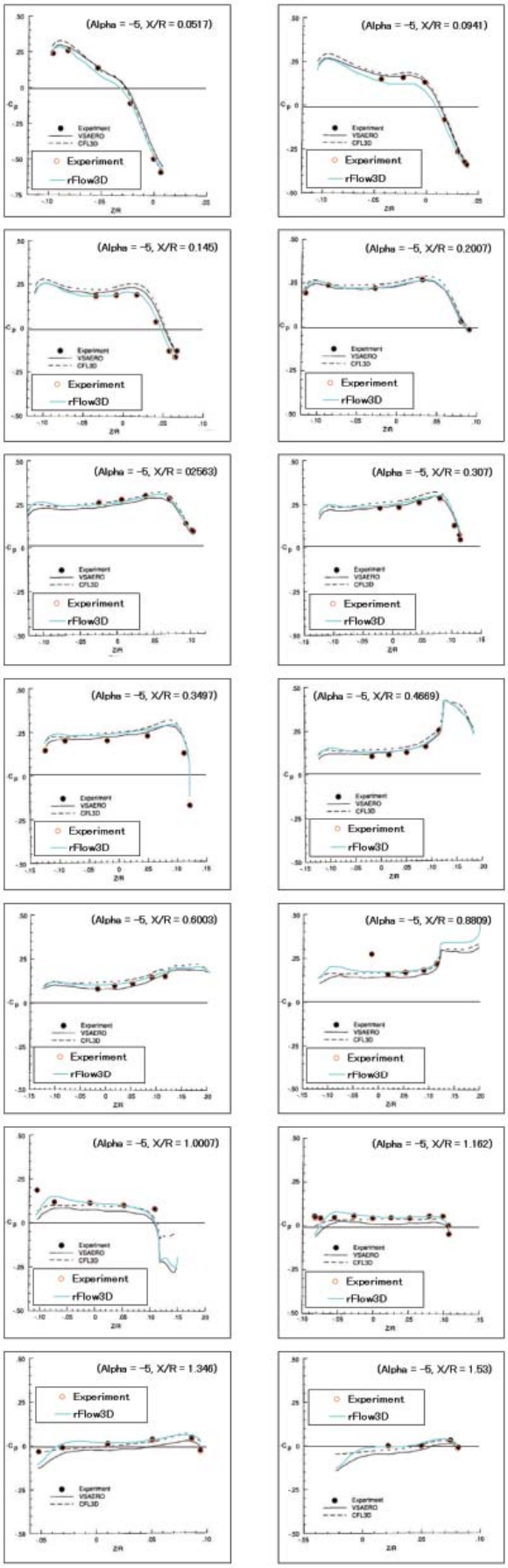

Fig. 6 Isolated fuselage surface pressure coefficients for $\alpha = -5^{\circ}$ [9]

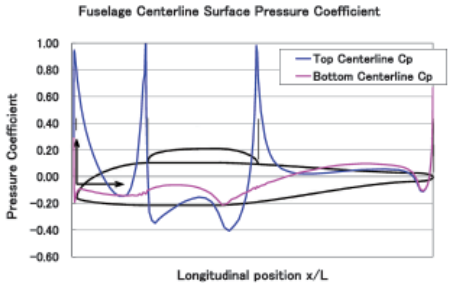

Fig. 7 Surface pressure coefficient along fuselage centerline for $\alpha = 0^{\circ}$

Table 1 ROBIN IRTS geometric features

Blade section	NACA 0012
Fuselage yaw	1.2°
Hub x/l coordinate	0.697
Hub y/l coordinate	0.051
Hub z/l coordinate	0.322

Table 2 Simulation blade control variables

Parameters	Fixed Control Cases		
Advance Ratio, μ	0.012	0.151	0.231
C_T/σ, *exp*	*0.0639*	*0.0656*	*0.0657*
C_T/σ, *CFD*	*0.0808*	*0.0747*	*0.0737*
M_∞	0.0066	0.083	0.127
M_{tip}	0.5533	0.5533	0.5533
α_s	0	-3	-3
β_o	1.5	1.5	1.5
θ_o	11.8	10.3	10.4
A_1,deg	-0.1	-2.7	-0.4
B_1,deg	0.2	2.4	3.8

in Table 1.

4.3 Thrust and Moment Coefficients

For the calculation of the rotor-fuselage combination simulating the flight conditions set in the reported experiments, the blade control variables were fix to the settings given by Mineck and Gorton. The resulting thrust and moment coefficients were then calculated and compared to the experimental settings.

The first cases calculated were for advance ratios of 0.012, 0.151 and 0.231, with a thrust coefficient of about 0.006. The computationally obtained thrusts are different from those measured experimentally using parameters listed in Table 2. Generally, control settings are changed to meet the measured thrust and moments. This method will be adopted in the next studies. Considering the reliabilities of the measurements of the controls and balances, validation with fixed controls has arguably equal importance.

The calculated history of the thrust coefficient for an advance ratio of 0.012 is shown in Fig. 8. In this case, the flight condition is nearly hovering and the downwash from the rotor acts on the fuselage and causes a downward load. The average thrust coefficient of the rotor itself is 7.892×10^{-3} and the download of the fuselage is -0.232×10^{-3} as defined in the same way as C_T. The total thrust (lift) coefficient is 7.66×10^{-3}. An isolated rotor case was calculated with the same rotor control settings which yielded a thrust coefficient of 7.835×10^{-3}. This value is lower than the rotor thrust with a fuselage by 0.7% but larger than the total lift value by 2%. It must be noted that the solver used here is an Euler solver and no friction that may cause under-estimation of the fuselage download was considered.

Fig. 9 shows the calculated thrust coefficients. The C_T value settles after about 1.5 rotor revolutions at slightly above 0.007. The difference with the predefined value of 0.0064 is still evident.

Also, moments around the rotor were obtained and plotted. The following diagrams show the rolling and pitching moment coefficients obtained from the simulations. For trimmed flight conditions, the magnitudes of these values need to be zero.

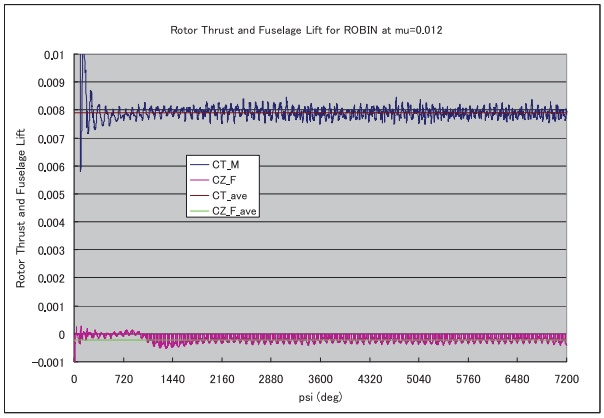

Fig. 8 History of thrust coefficient for μ = 0.012

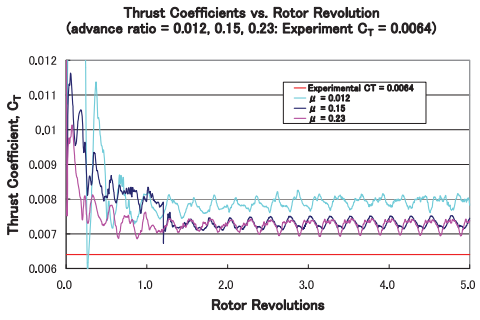

Fig. 9 History of thrust coefficients for μ = 0.012, 0.15 and 0.23

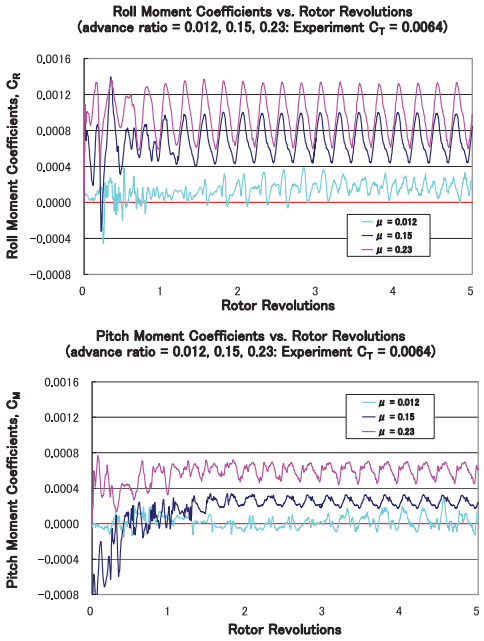

Fig. 10 Moment Coefficients at μ = 0.012, 0.15 and 0.23

4.4 Iso-Surface Plots

The simulation data was visualized as iso-surface plots for the criterion-Q values depicting the rotor wake. The visualization permitted a qualitative analysis of the rotor-fuselage interaction features in the flow field. The flow features around the rotor blade root and in other low speed areas were improved after application of the modified SLAU scheme to the solver, as could be expected from the previous validation results [5, 17]. Fig. 11 shows the iso-surface plots of criterion-Q values of 1.5 of the simulation for the advance ratio of 0.012

The rotor wake at this low advance ratio engulfs most part of the fuselage, while at forward flying conditions shown in the following figures, the wake impinges only the rear part of the tail boom. Figs. 12 and 13 show the iso-surface plots of criterion-Q

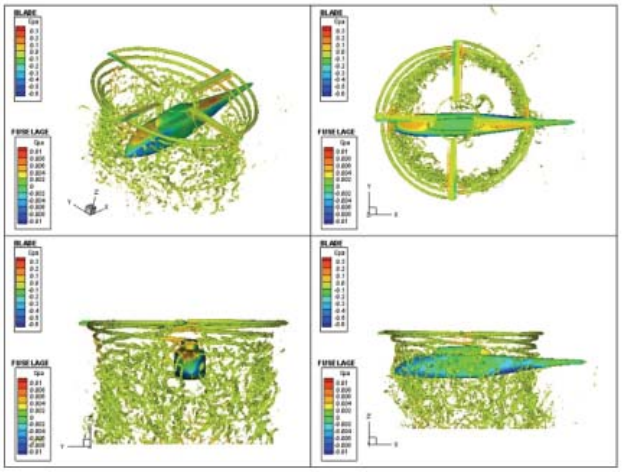

Fig. 11 Iso-surface plot of criterion-Q = 1.5 for μ = 0.012

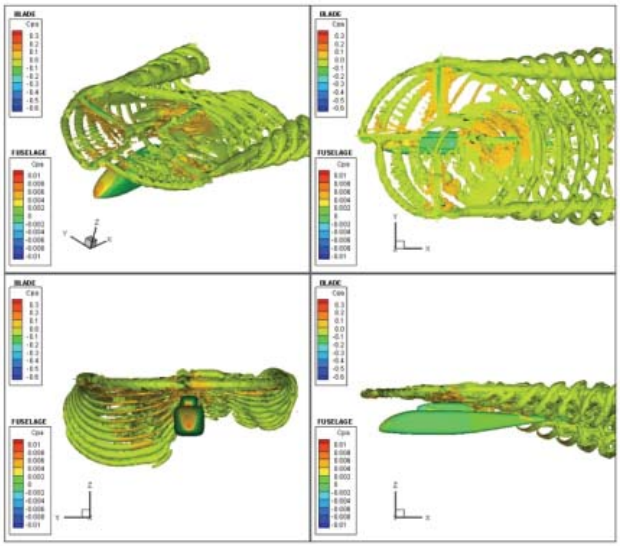

Fig. 12 Iso-surface plot of criterion-Q = 0.05 for μ = 0.15

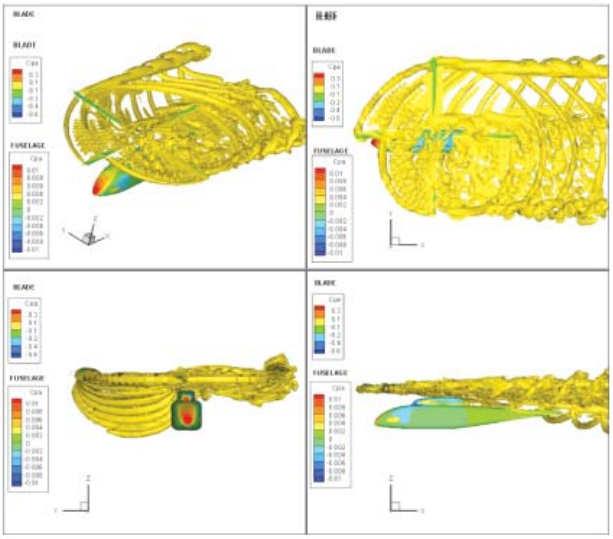

Fig. 13 Iso-surface plot of criterion-Q = 0.05 for μ =0.23

values of 0.05 of the simulation for advance ratios of 0.15 and 0.23, respectively.

4.5 Periodic Pressure Coefficient Results

The surface C_P results were extracted at the same points of the pressure taps shown in Fig. 14 to compare them with experimental results reported by Mineck and Gorton [7]. The pressure tap location distributions follow either a constant longitudinal position cross-sectional distribution or a top centerline distribution. For the cross-sectional distribution, the chosen longitudinal station is at an x/l position of 0.9, with the z-directional positions defined in the NASA experiment report [7].

The averaged values of C_p at each pressure tap location have been obtained and compared with the experimental results. The results are shown in Fig. 15 for measurement locations along

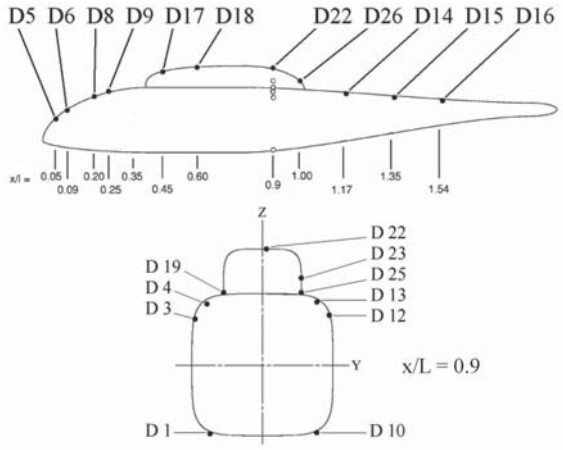

Fig. 14 Pressure tap positions at x/L = 0.9 and top-centerline [7]

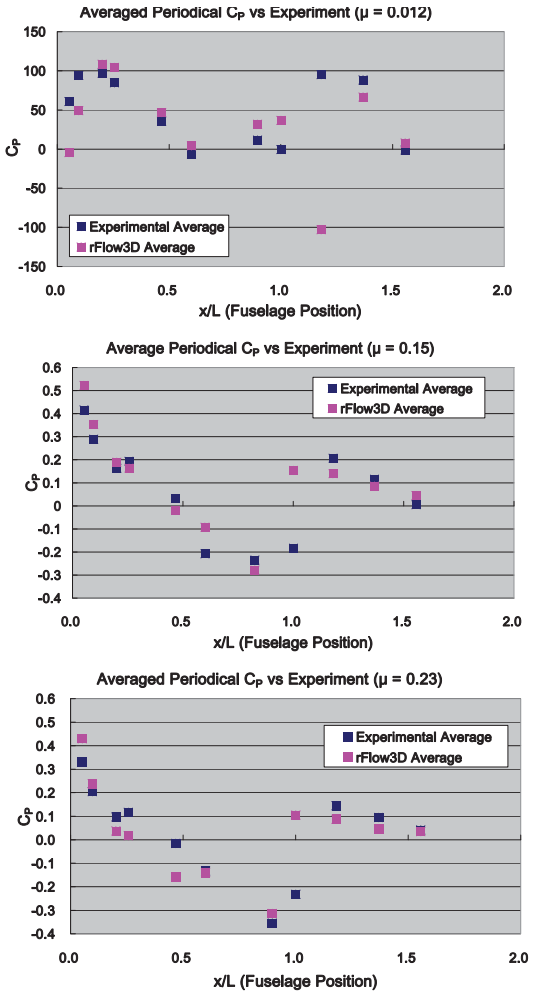

Fig. 15 Averaged Periodical C_p Values at Longitudinal Positions for μ = 0.012, 0.15 and 0.23

the top centerline, as defined in Fig. 14. The magnitude of the respective values at each position generally match except for the position close to x/l = 1.0, where some effects due to flow separation are occurring near the blunt rear end of the engine housing structure.

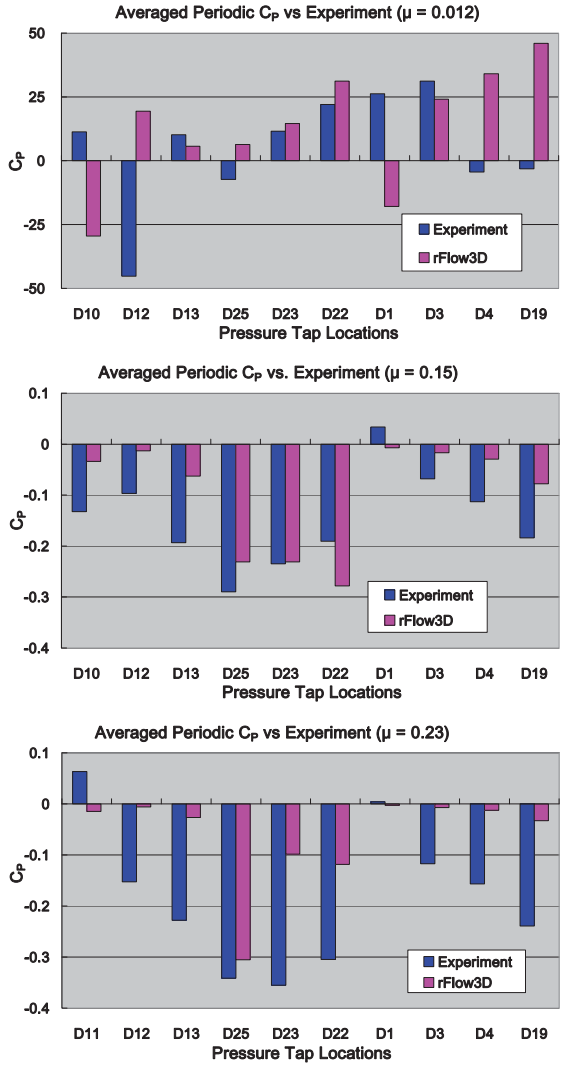

Fig. 16 Averaged Periodical C_p Values at x/L = 0.9 for μ = 0.012, 0.15 and 0.23

The same set of data was compared for positions around the cross section at x/L = 0.9 (Fig. 16.) The discrepancy evident at these pressure tap locations could be due to the proximity to the blunt rear end of the engine housing structure, where effects caused by flow separation are presumably occurring, as aforementioned.

The following figures show the comparison between calculation and experiment of the fuselage surface periodical C_p fluctuations at the respective advance ratios of 0.012, 0.15 and 0.23. For each advance ratio, the first set of figures shows results at the fixed longitudinal station of x/l = 0.9, while the second set shows results along the top centerline. The pressure coefficient fluctuation values are plotted for one entire rotor revolution with the azimuth angle going from 0 to 360 degrees. The experimental data was shifted by a phase of 28 degrees to account for the lag between the azimuthal blade position measurement and the pressure recording [16, 18].

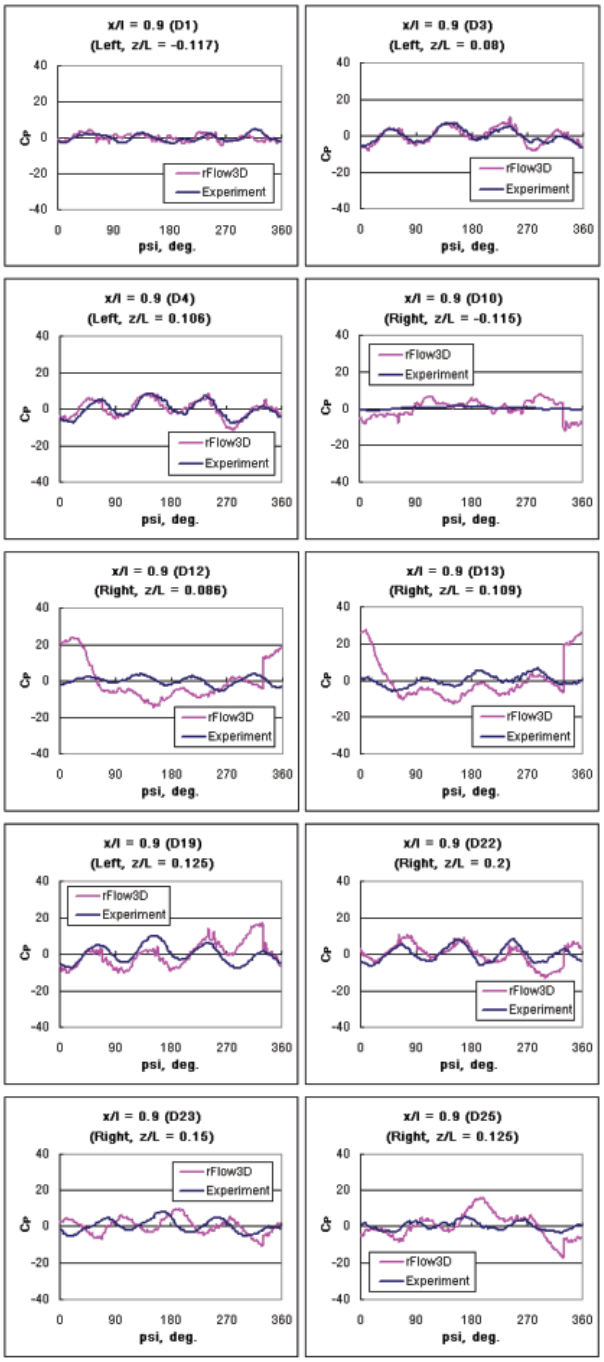

Fig. 17 C_p vs. experiment at x/L = 0.9 for μ = 0.012

For the case of the advance ratio of 0.012, while some of the figures show agreement between simulation and experiment, in many others the discrepancy is still evident. In some of the positions on the fixed longitudinal station of x/l = 0.9, it is likely that even after many rotor revolutions, the wake has not reached a steady state, as is seen from the non-periodical fluctuation of the pressure coefficient values, shown in Figure 17.

At advance ratios of 0.15 and 0.23, the surface pressure fluctuations seem to have reached a steady state. For the case μ = 0.15,

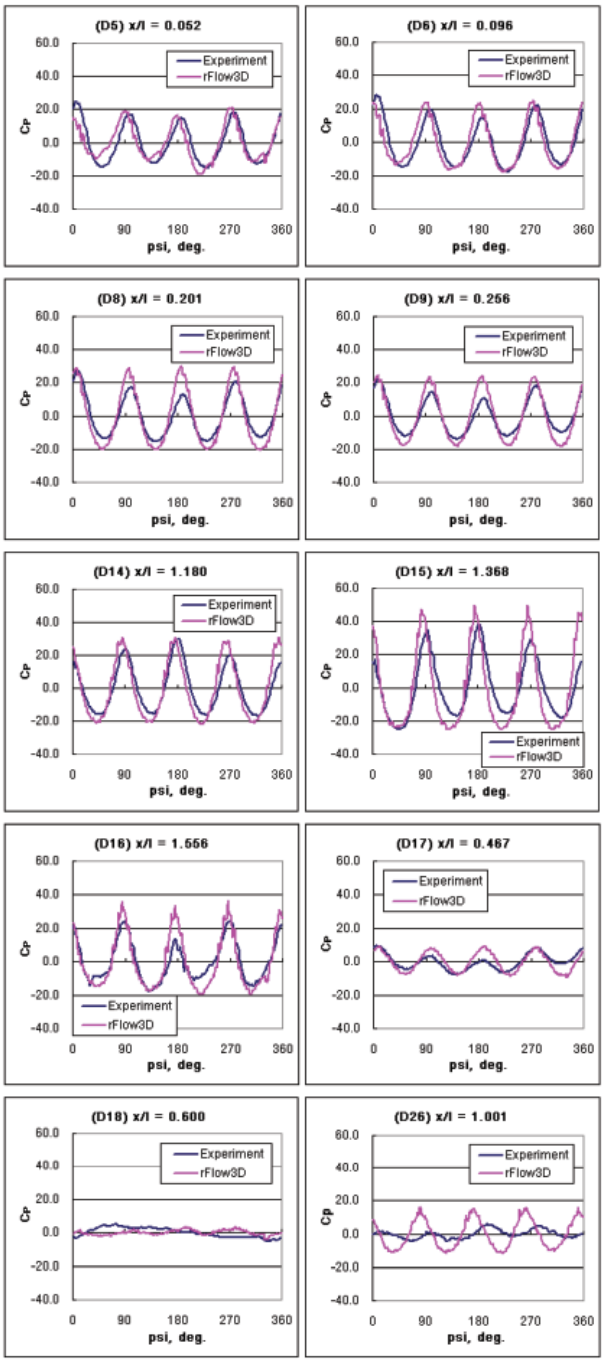

Fig. 18 C_p vs. experiment at Top-centerline for $\mu = 0.012$

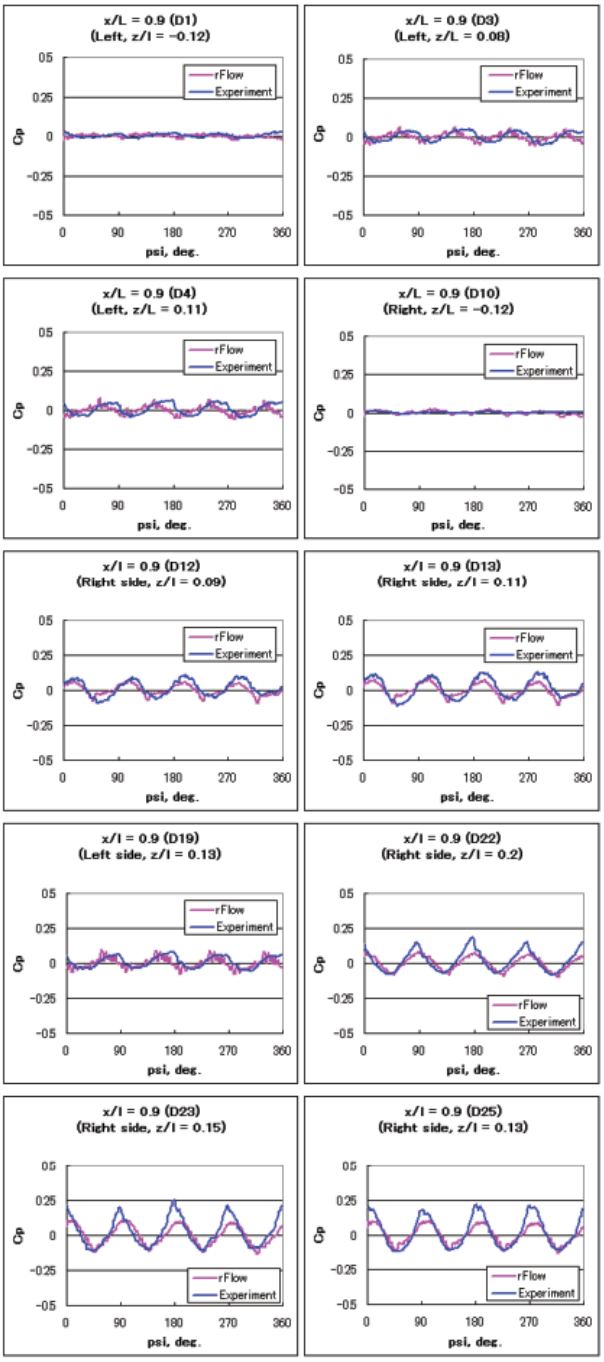

Fig. 19 C_p vs. experiment at x/L = 0.9 for $\mu = 0.15$

the phases roughly match and the magnitude of the amplitudes seem to be similar between results at positions around the ring at x/L = 0.9. The trend of the amplitudes roughly matches, decreasing at lower positions (Fig. 19.)

The diagrams in Fig. 20 show the same values taken at the top center line of the fuselage. The results in Fig. 20 show that the discrepancy in phase is small, except for that at position x/l = 1.001 where the difference is most noticeable. The trend of the amplitude magnitude appears to overpredict at positions forward the rotor, and to underpredict aft of it.

The results for $\mu = 0.23$, shown in Figures 21 and 22, indicate the same tendencies of the shift in phase between calculation and experiment. Again, there is only a rough agreement in the C_P fluctuation amplitude.

These results show that the simulation results are generally reliable, though some adjustment to match the periodic C_p fluctuation phase may be needed at some positions. The effects due to viscosity existing in the experimental measurements, which

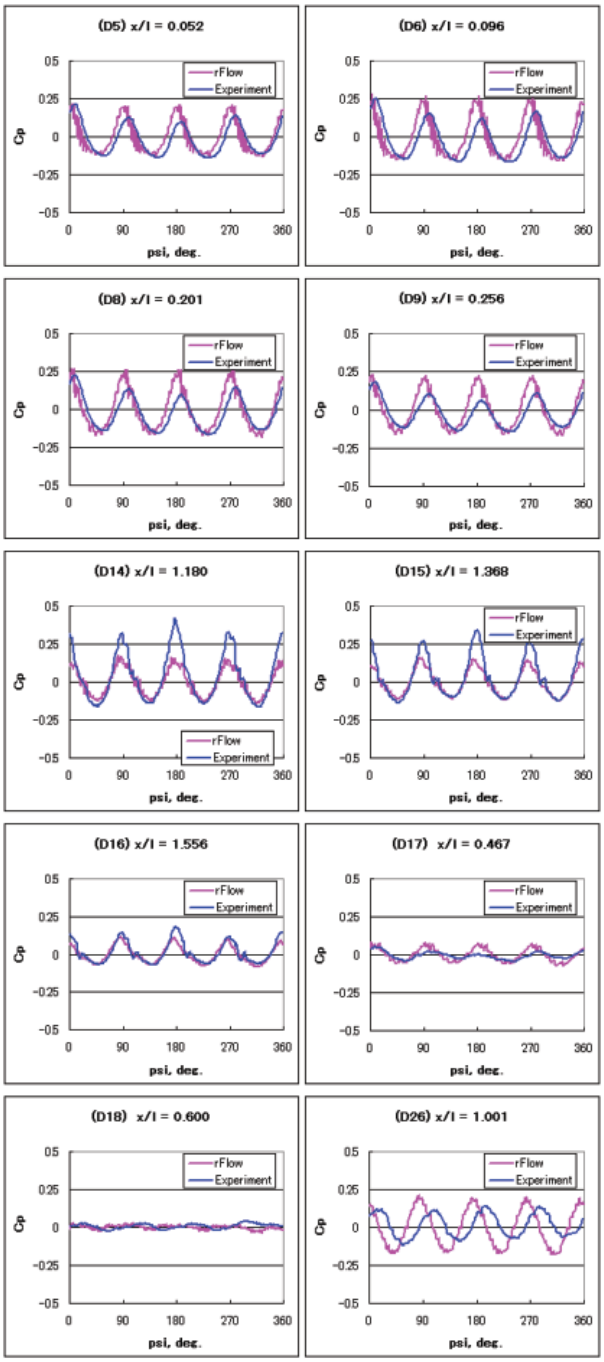

Fig. 20 C_p vs. Experiment at Top-centerline for $\mu = 0.15$

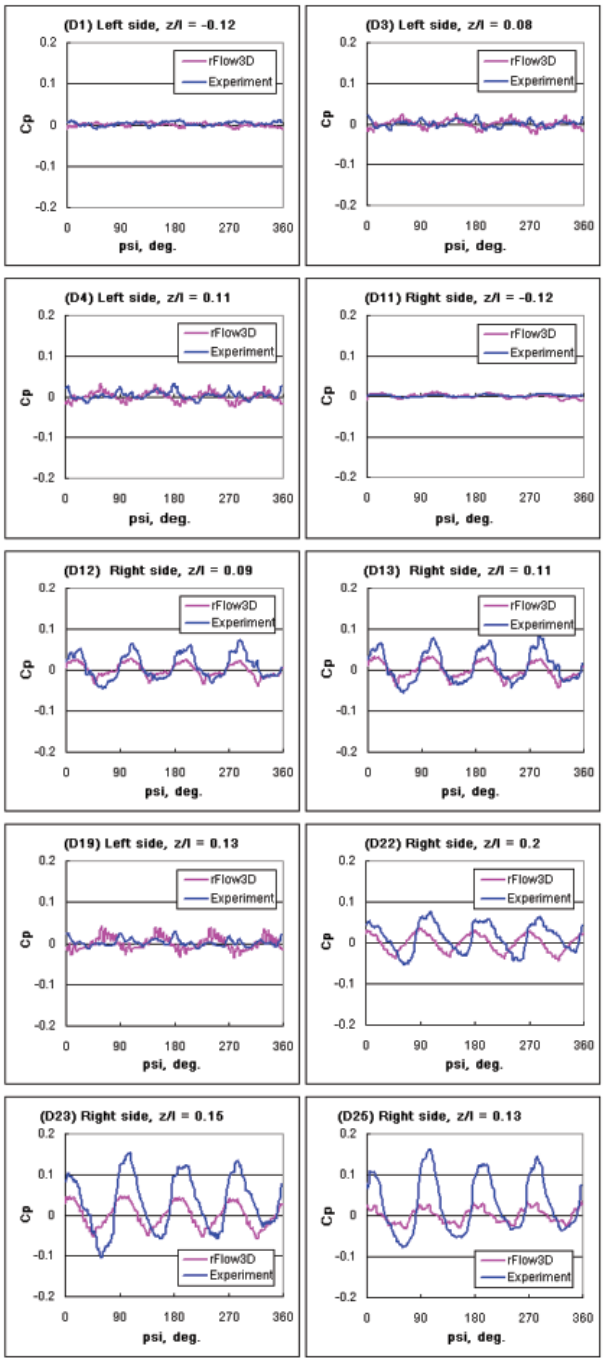

Fig. 21 C_p vs. experiment at x/L = 0.9 for $\mu = 0.23$

are not taken into account in the computations using the Euler solver, seem to cause only little discrepancy between numerical and experimental results.

5. CONCLUSIONS

A new rotor flow solver; *rFlow3D* developed in JAXA is used to calculate the ROBIN test cases. Flow features around the rotor blade root and in other low speed areas are improved after applying the modified SLAU scheme to the solver. For the isolated case, the obtained pressure on the fuselage surface agrees well with the experimental results except at the aft-body area, where effects due to viscosity are not considered, as the calculations were executed with an Euler solver.

Test calculations for the ROBIN rotor/fuselage combination are carried out and reasonably good agreements with the experimental results are obtained. As the next step for the analysis of rotor/fuselage interaction, an attempt will be made to calculate

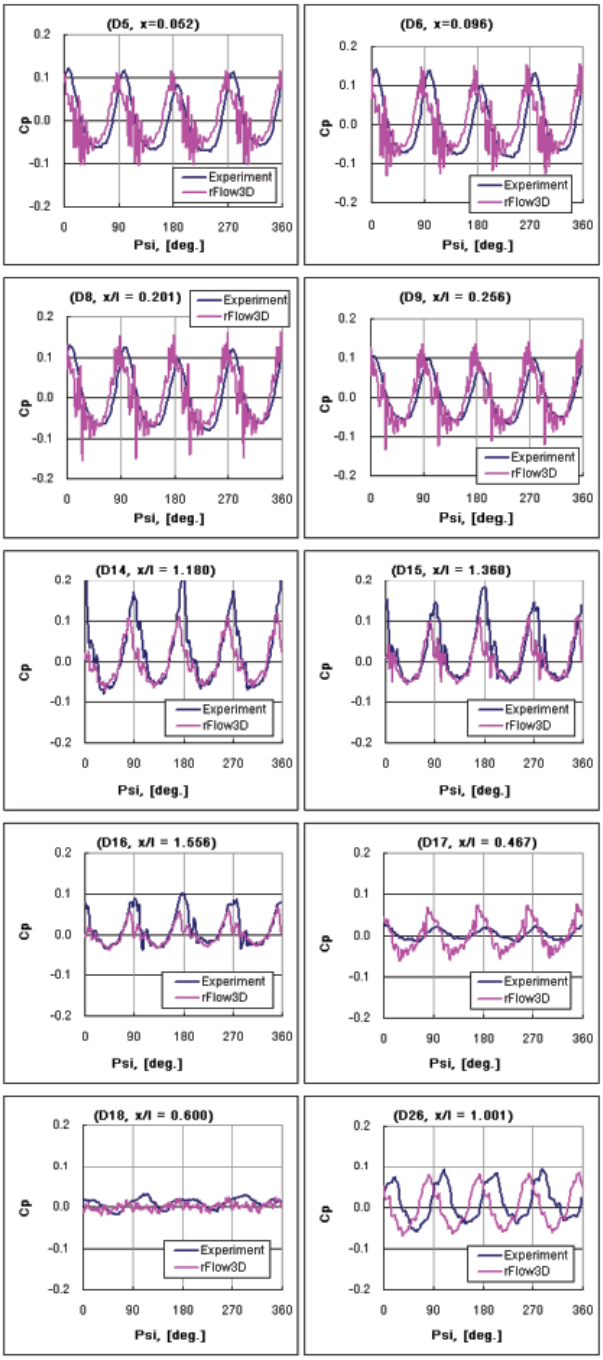

Fig. 22 C_p vs. experiment at Top-centerline for $\mu = 0.23$

the trimmed cases, where the rotor control parameters are varied during the computation to attain the predefined thrust and moment coefficients. We concluded that the newly developed *rFlow3D* solver should be promising for future applications in the analysis of flow fields around helicopters.

ACKNOWLEDGMENTS

The authors would like to thank Mr. Hideaki Sugawara of Ryoyu Systems Co., Ltd., Nagoya, Japan, for assistance during the set up and data visualization process.

REFERENCES

[1] E. Shima and K. Kitamura, "On New Simple Low-Dissipation Scheme of AUSM-Family for All Speeds," 47th *AIAA Aerospace Sciences Meeting*, Orlando, FA, January 5-8 2009. *AIAA Paper* 2009-136.

[2] Shima, E. & Kitamura, K., "On AUSM-Family Scheme for All Speeds with Shock Detection for Carbuncle-Fix," *19th AIAA CFD, 22-25 June 2009, San Antonio, Texas*, *AIAA Paper* 2009-3544.

[3] Y. Tanabe and S. Saito, "Significance of All-Speed Scheme in Application to Rotorcraft CFD Simulations," *The 3rd International Basic Research Conference on Rotorcraft Technology, Nanjing, China*, October 14-16, 2009.

[4] M.S., Liou, "A Sequel to AUSM, Part II: AUSM+-up for All Speeds," *J. Comp. Phys*., Vol. 214, pp. 137–170, 2006.

[5] Y. Tanabe, S. Saito and I. Otani, "Application of SLAU Scheme to Helicopter CFD," *41st Fluid Dynamics Conference/Aerospace Numerical Simulation Symposium 2009*, Chofu, Tokyo, June 18-19 2009 (In Japanese.)

[6] C. E. Freeman and R. E. Mineck, "Fuselage Surface Pressure Measurements of a Helicopter Wind Tunnel Model with a 3.15 Meter Diameter Single Rotor," *NASA TM 80051*, March 1979.

[7] R. E. Mineck and S. A. Gorton, "Steady and Periodic Pressure Measurements on a Generic Helicopter Fuselage Model in the Presence of a Rotor," *NASA TM-2000-210286*, June 2000.

[8] H., Luo, J., Baum & R., Lohner, "On the Computation of Multi-Material Flows Using ALE Formulation," *Journal of Computational Physics*, Vol. 194, pp. 304–328, 2004.

[9] M. S. Chaffin and J. D. Berry, "Navier-Stokes and Potential Theory Solutions for a Helicopter Fuselage and Comparison With Experiment," *NASA TM 4566*, June 1994.

[10] M. J. Wright, G. V. Candler and M. Prampolini, "Data-Parallel Lower-Upper Relaxation Method for the Navier-Stokes Equations," *AIAA Journal*, Vol. 34, No. 7, July 1996.

[11] S., Yamamoto & H., Daiguji, "Higher-Order-Accurate Upwind Schemes for Solving the Compressible Euler and Navier-Stokes Equations," *Computers & Fluids*, Vol. 22, No. 2/3, pp. 259–270, 1993.

[12] Zhang, L.P. & Wang, Z.J., "A Block LU-SGS Implicit Dual Time-Stepping Algorithm for Hybrid Dynamic Meshes," *Computers & Fluids*, Vol. 33, pp. 891–916, 2004.

[13] M. J. Wright, G. V. Candler and M. Prampolini, "Data-Parallel Lower-Upper Relaxation Method for the Navier-Stokes Equations," *AIAA Journal*, Vol. 34, No. 7, July 1996, pp. 1371–1377.

[14] Tanabe, Y. & Saito, S., "A Simplified CFD/CSD Loose Coupling Approach for Rotor Blade Deformation," *JAXA-RR-08-008E*, 2009.

[15] M. S. Chaffin and J. D. Berry, "Navier-Stokes and Potential Theory Solutions for a Helicopter Fuselage and Comparison With Experiment," *NASA TM 4566*, June 1994.

[16] A. R. Kenyon and R. E. Brown, "Wake Dynamics and Rotor-Fuselage Aerodynamic Interactions," *AHS 63rd Annual Forum*, Virginia Beach, VA, May 1-3 2007.

[17] Y. Tanabe, S. Saito and H. Sugawara, "Validation of High Resolution CFD Analysis For Flowfield Around a Rotor," *47th Aircraft Symposium*, Gifu, Japan, November 4-6, 2009 (In Japanese.)

[18] D. M. O'Brien, "Analysis Of Computational Modeling Techniques For Complete Rotorcraft Configurations," *PhD thesis*, Georgia Institute of Technology, May 2006.